Joint inversion of the first overtone and fundamental mode for deep imaging at the Valhall oil field using ambient noise

Gaurav Tomar,[1,*] Eleonore Stutzmann,[1] Aurelien Mordret,[2] Jean-Paul Montagner,[1] Satish C. Singh[1] and Nikolai M. Shapiro[1]

[1]*Institut de Physique du Globe de Paris, Sorbonne Paris Cité, CNRS (UMR* 7154*), Paris, France. E-mail:* gtomar@dias.cp.ie
[2]*Earth Resources Laboratory, Department of Earth, Atmospheric and Planetary Sciences, MIT, Cambridge, MA 02139, USA*

SUMMARY

Surface waves derived from ambient noise data are composed of fundamental and higher modes. The first overtone is sensitive to structure from the surface down to a greater depth than the fundamental mode. We use 6.5 hr of continuous recording of noise on 2320 ocean bottom cable sensors from the Valhall Life of Field Seismic and we compute the intersensor cross-correlation functions for the vertical and radial components. We observe that the vertical component is dominated by the fundamental mode whereas on the radial component, the first overtone is stronger than the fundamental mode. Forward modelling demonstrates that a few hundred metres of low velocity sediments along with the water layer plays an important role for the generation of stronger first overtone signal on radial component. When we invert only the fundamental mode phase velocity data, the *S*-wave velocity model has vertical resolution down to 600 m depth. Combining the fundamental mode and the first overtone enables to image deeper structure down to 1 km depth, highlighting the presence of a low velocity zone.

Key words: Interferometry;.

1 INTRODUCTION

Seismic interferometry has made it possible to convert noise data into signal by cross-correlating noise data recorded at two stations (e.g. Weaver & Lobkis 2001a,b; Roux *et al.* 2004; Shapiro & Campanile 2004; Snieder 2004, 2006; Wapenaar 2004; Roux & Sabra 2005; Wapenaar & Fokkema 2006; and Gouédard *et al.* 2008). Ambient seismic noise is the continuous oscillation of the Earth that is recorded worldwide and contains information about the subsurface structure. The deterministic signal extracted from cross-correlations (CCs) of seismic noise is complementary to earthquake seismograms. The main source of seismic noise in the period band 1–10 s is known as secondary microseisms. They are generated by the interaction of the ocean gravity waves of similar frequencies that travel in opposite directions (Longuet-Higgins 1950; Hasselman 1963).

Most applications of ambient noise tomography have shown high-resolution images of the crust and the upper mantle at different scales (e.g. Shapiro *et al.* 2005; Moschetti *et al.* 2007; Yang *et al.* 2007; Bensen *et al.* 2008; Nishida *et al.* 2009; Ekström *et al.* 2009; Haned *et al.* 2015). Also, noise CC approach has been applied to extract reflection responses from industrial seismic networks

(Draganov *et al.* 2007, 2013). The green's function extracted from the ambient noise is also used in Kanto basin (e.g. Viens *et al.* 2016). For very shallow structures, the seismic noise data sets have been extensively used in the past few years, particularly after installation of Valhall array (e.g. de Ridder 2011, 2014; de Ridder & Biondi 2013; Mordret *et al.* 2013a,b,c, 2014a,b; de Ridder *et al.* 2014; Tomar *et al.* 2015a,b, 2016).

In most of these studies, only the fundamental mode of surface waves is retrieved because it is easily extracted from noise CCs of vertical component. Using stations in a sedimentary basin, Savage *et al.* (2013) observed stronger first overtone than the fundamental mode for radial–radial CCs. In oceanic environment, Gualtieri *et al.* (2015) investigated the complexity of waveforms in 2-D models and showed variations of the strongest mode recorded on the vertical component along the profile. Here, in the oceanic area of Valhall, we observe that the first overtone signal is stronger than the fundamental mode on the radial-radial CCs. (Tomar *et al.* 2015b). At the ocean bottom, depending on the period and velocity of the medium, we record either Scholte or Rayleigh waves. Scholte wave amplitude is maximum at the interface, and it decreases exponentially above and below it (Scholte 1946; Scholte 1947; Scholte 1958). The interface wave at a boundary between vacuum/air and solid is called Rayleigh wave. The physics is similar for Scholte and Rayleigh waves but the Scholte wave phase velocity is lower than the lowest velocity in the medium [for example, in ocean-sediment medium, these waves

* Now at: Dublin Institute for advanced studies, 5 Merrion Square, Dublin 2, Ireland.
*

propagate with phase velocity much lower than the sound velocity in water (Biot 1952)]. Scholte waves become Rayleigh waves at long period.

Recently, several studies have shown the potential to extract higher modes of surface waves from the noise CCs (Socco & Strobbia 2004; Harmon *et al.* 2007; Nishida *et al.* 2008; Rivet *et al.* 2015). Overtones are of great interest because they are sensitive to deeper structures than the fundamental mode at the same frequency hence, improve depth resolution (Kimman & Trampert 2010; Rivet *et al.* 2015). Higher modes are observed reasonably often, when very shallow structures are examined. They just are generally considered to be a problem and are avoided rather than used (e.g. Boaga *et al.* 2013).

Here, we first consider the average CC function for the Valhall Life of Field Seismic dataset and we measure the dispersion curve for the fundamental mode and the first overtone on the vertical and radial components, respectively. We invert these dispersion curves to derive the average S-wave velocity model. This model is then used to investigate the corresponding seismic wavefield and to explain the relative amplitude of the fundamental mode and the first overtone. We then measure dispersion curves across the Valhall Life Field Seismic array for the fundamental mode and for the first overtone. We perform a depth inversion using neighbourhood algorithm (NA) (Sambridge 1999) and compare model obtained from the fundamental mode alone with the model obtained using both the fundamental mode and the first overtone.

2 DATA AND CROSS-CORRELATION

In 2003, BP installed a permanent network of ocean bottom cable (OBC), called 'Life of Field Seismic' (LoFS) to monitor the reservoir. It was the world's largest permanent OBC (of ~120 km long) seismic array at the time of its installation. We were provided continuous recording of 6.5 hr of ambient seismic noise on four component sensors (Z-vertical, N-north, E-east components of the seismometer and H-hydrophone) at Valhall LoFS network (Fig. 1) for this study. We use ambient noise recorded on vertical and radial components. The data set was recorded at 250 samples per second on 2320 sensors where the interstation distance between them along the cable was 50 m and intercable distance was 300 m. Fig. 2 shows the virtual gathers that are obtained by stacking all CCs (~2 690 040) computed for individual component that fall into a 10-m interstation distance bin. Stronger fundamental mode can be seen in the virtual gather of the vertical component CCs (Fig. 2a) and stronger first overtone signal in the virtual gather of radial component CCs (Fig. 2b).

3 INVERSION OF AVERAGE DISPERSION CURVES

We first invert for average 1-D S-wave velocity model of Valhall before inverting for 3-D model. F–K analysis (Gabriels *et al.* 1987) of virtual gathers is performed for the vertical and radial components to measure the average dispersion curves for the fundamental mode and the first overtone of Scholte/Rayleigh waves. The dispersion curves can be measured by picking the maximum energy for each mode (Figs 2c and d). The virtual gather for hydrophone–hydrophone (HH) cross-correlation and F–K spectrum are also computed (see Supporting Information Fig. S1) and compared with vertical and radial component cross-correlations. The hydrophone
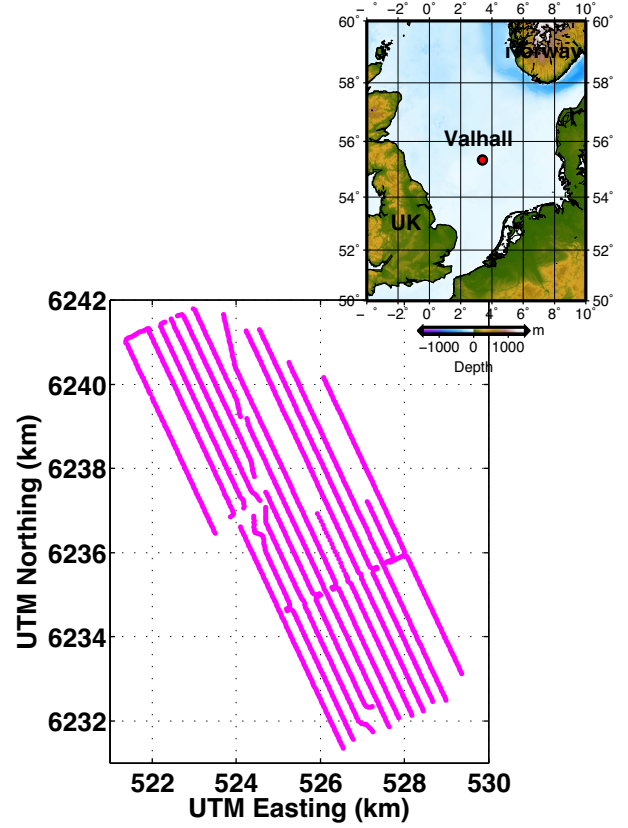
Figure 1. Map of Valhall LoFS array. Each magenta colour point indicates a 4C sensors. The geographical location of Valhall oil field is shown with the red dot in inset.

CCs have the same behaviour as the radial component CCs with a stronger first overtone signal.

The maximum energy from F–K spectrum of vertical component virtual gather is picked and superimposed on the F–K spectrum of radial component virtual gather. Dispersion curves of fundamental mode and first overtone have the same speed on both the radial and vertical components. Hence, on the horizontal component, the first overtone signal belongs to the Scholte/Rayleigh waves, they are not due to the coupling of Love wave signal. The phase velocity, *c,* can be obtained for a frequency *f* and a wavenumber *k* using the following equation:

$$c_m (f) = \frac{2\pi f}{k_{m(f)}} \,, \tag{1}$$

where *m* is the mode number. We then fit these measurements with a third-order polynomial to obtain smoothed dispersion curves (solid lines in Fig. 3a). The dispersive property can be easily identified as the velocity increases with increasing periods of both modes.

When the F–K analysis is performed to the entire data set, average phase velocities can be measured in the frequency range 0.55–1.7 Hz (period 0.58–1.8 s) for the fundamental mode and in the frequency range 0.6–1.2 Hz (period 0.8–1.6 s) for the first overtone (Fig. 2). For tomography (Section 5), only subsets of data are used for each F–K analysis and the phase velocities can be measured only in the narrower frequency range: 0.625–1.42 Hz (period 0.7–1.6 s) for the fundamental mode and 0.655–1 Hz (period 1–1.5 s) for the first overtone. These dispersion curves are used to perform depth inversion in the next section.
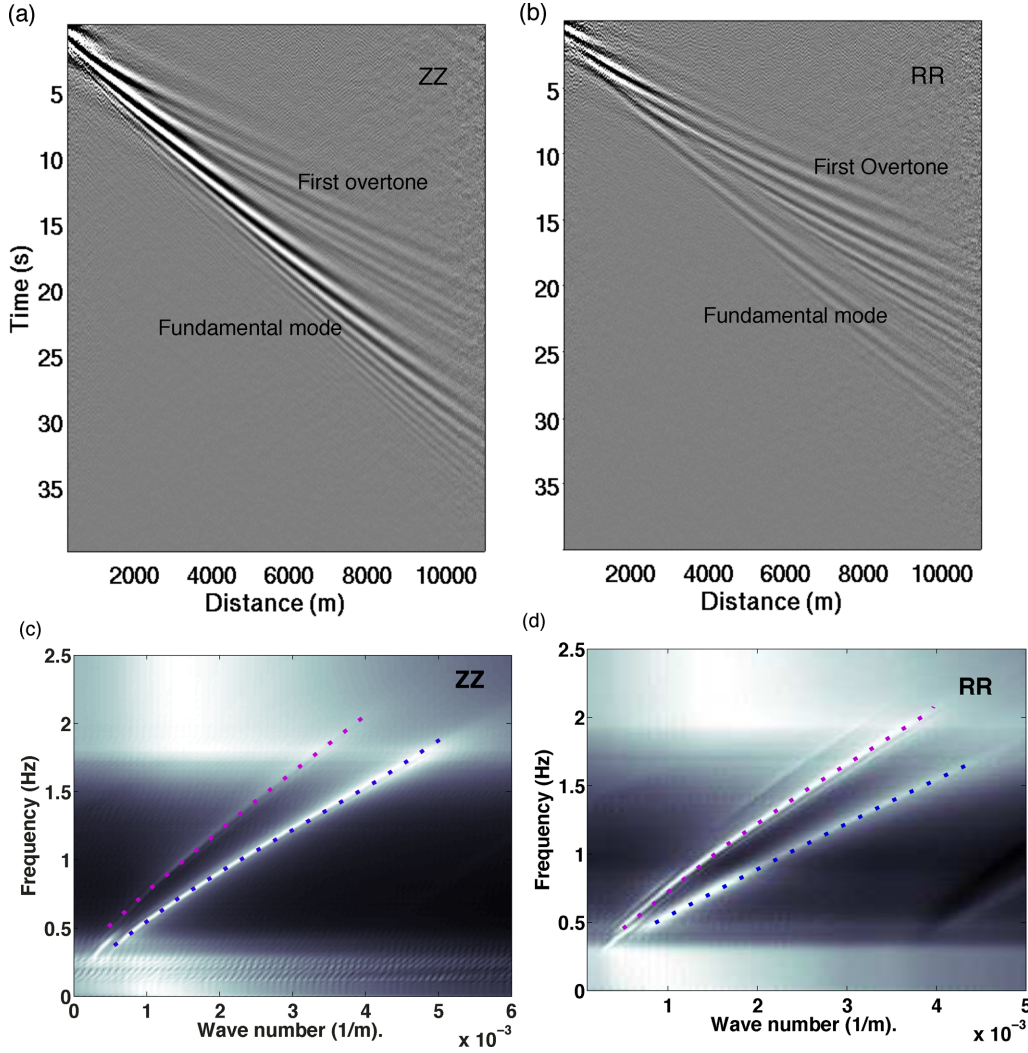
Figure 2. Virtual gather (a) and its F–K spectrum (b) of ZZ component. Virtual gather (c) and its F–K spectrum (d) of RR component. All the correlations computed for ZZ and RR component are stacked and averaged in 10 m interstation distance bins. Blue and magenta colour are the fundamental mode and the first overtone dispersion curves, respectively, that are picked from the F–K spectrum.
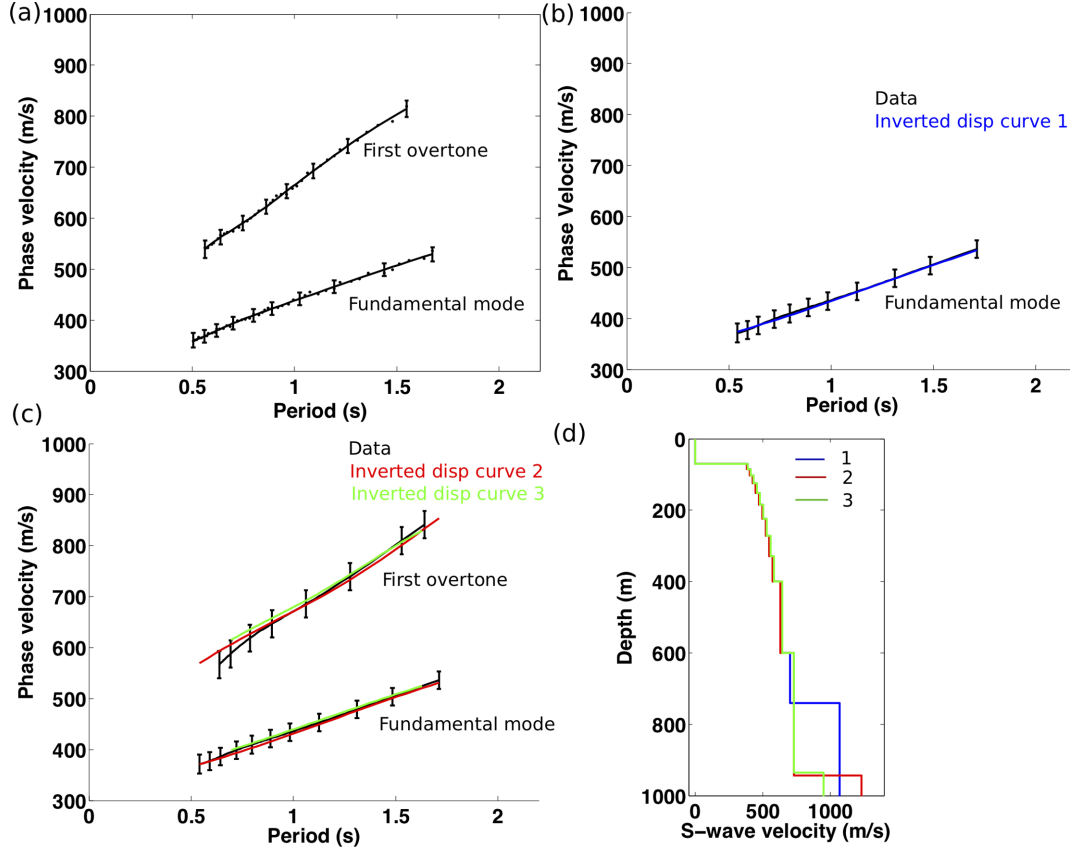
3.1 Inversion of average dispersion curves with using the neighbourhood algorithm (NA)

We invert the Scholte/Rayleigh wave average dispersion curve with a method based on the NA (Sambridge 1999) already used by Mordret *et al.* (2014a) and Tomar *et al.* (2016). For an isotropic medium, the model is most often parametrized as a 1-D layered $\underline{S}$-wave velocity profile, where parameters are the thicknesses and velocities (that are constant) in each layer. Here, we only invert S-wave velocity because we assume low sensitivity of surface wave to P-wave velocity and density. Therefore, the P-wave velocity and density are scaled from the empirical relation: $V_p = 1.16V_s + 1.36$ (Castagna *et al.* 1985) and $\rho = 1.74(V_p)^2$ with V_p in km s^{-1} (Brocher 2005). The S-wave velocity model consists of a fixed water layer at the top, several layers of varying velocity and thickness and a half-space at the bottom. The average water depth at Valhall is 70 m. Information about the subsurface structure of Valhall is available from well loggings and active source seismic data sets (e.g. Barkved 2012) and a 3-D P-wave velocity model (Sirgue *et al.* 2010a,b). Using these information and stratigraphic logs (Munns 1985), it has been established that there are unconsolidated sediments of a few hundred metres. There are two structural discontinuities at 600 and 950 m

depths. We use this information to simplify the model parametrization for the S-wave velocity. To reduce the number of parameters in the inversion, we use a power-law equation, from seafloor down to 600 m, the S-wave velocity, V_S at depth d is parametrized as follows (Wathelet 2004):

$$V_s(d) = V_0\left((d+1)^\alpha - (d_0+1)^\alpha + 1\right), \tag{2}$$

where V_0 is the velocity just below the seafloor, α is the power-law parameter, d_0 is the water depth (for Valhall it is 70 m). Below 600 m, we add one layer of varying thickness and velocity and a half-space. We invert four parameters: S-wave velocity below the sea floor V_0, and the power-law parameter α in eq. (2), the velocity and thickness of the layer below 600 m. The NA algorithm has several steps, first we generate n_1 1-D randomly generated S-wave velocity models in the model space, then we create a mesh of Voronoi cells that are used to combine these models. For each model, theoretical dispersion curve is computed (Herrmann & Ammon 2004) and a misfit between theoretical and observed dispersion curves is assigned to each cell (Mordret *et al.* 2014a). Second, we choose the best n_c cells on the basis of best misfit and new models n_s are generated. Then, we generate a new set of Voronoi

Figure 3. (a) Average phase velocity dispersion curves. Black dots are phase velocity picks measured on the F–K spectra (Figs 2c and d) for the fundamental and first overtone, respectively. Black solid lines with error-bars are the third order polynomial fits of these phase velocities. (b) Comparison between measured (black) and inverted (blue) phase velocities when only the fundamental mode is inverted. (c) Comparison between measured (black) and inverted (green and red) velocities when both fundamental mode and first overtone are inverted. (d) inverted *S*-wave velocity as a function of depth for the three inversions: when only the fundamental mode is inverted (blue); when the fundamental mode and first overtone are inverted in the period range 0.55 to 1.75 s (red); when the fundamental mode and first overtone are inverted in the period range 0.7 to 1.6 s and 1 to 1.5 s, respectively (green).

cells on the basis of new and previous models. Finally, we repeat this last procedure to n_i iterations. The code used to compute the synthetic dispersion curves (Herrmann & Ammon 2004) requires a set of layers with constant elastic properties to define the structure. Therefore, we choose 13 thin layers to approximate the Valhall structure and the velocities in each layer are selected to fit eq. (2). The bounds on the parameters are [150– 500] m s^{-1} for V_0, [0.8– 2.3] for α [500–1400] for depth d_{n-1} and [500–1500] m s^{-1} for V_{n-1} (velocity of 13th layer). The NA was run with $n_1 = 10\ 000$, $n_s = 1000$, $n_c = 5$ and $n_i = 8$. We tested 50 000 models using NA.

Among these 50 000 models, we choose the best 1000 models and take their average to get the final 1-D *S*-wave velocity model. The 1000 best models are selected based upon their misfit function (Mordret *et al.* 2014a). The average of these models is not very different from the model that achieves the best misfit, while it may provide a more stable solution than just selecting one model based only upon the best misfit (Tomar *et al.* 2016).

We performed three inversions to test the influence of using the first overtone in the two frequency ranges where it could be measured. The first inversion was performed using only the average fundamental mode dispersion curve in the period range 0.55–1.75 s (black colour curve with error bar on Fig. 3b). The average of the 1000 best-fitting *S*-wave velocity models is shown in Fig. 3(d)— model 1, blue curve—and the corresponding phase velocity on Fig. 3(b)—blue curve. One can see that the fundamental mode has

limited sensitivity to structure deeper than 700 m. Then, a second inversion was performed using the average phase velocities for the fundamental mode and first overtone in the period range 0.55–1.75 and 0.7–1.6 s, respectively (red curves corresponding to model 2, in Figs 3c and d). In this inversion, we found a second discontinuity at ∼950 m depth. Finally, the third inversion was performed using the two modes in the narrow frequency band in which they could be measured locally for every grid point (and used in Section 5 for tomography). These period ranges are 0.7–1.6 s for the fundamental mode and 1–1.5 s for the first overtone (green curves corresponding to model 3, in Figs 3c and d). All three models are similar down to 700 m. Models 2 and 3 are similar down to 950 m. Only the velocity deeper than 950 m is larger when the first overtone dispersion curve is inverted in the wide period range.

The average velocity model 2 (hereafter called Valhall) is used for the synthetic modelling in the next section and as a starting model for the tomographic inversion in Section 5.

4 SYNTHETIC SEISMOGRAM MODELLING

In this section, we model synthetic seismograms to investigate why the fundamental mode and the first overtone are the dominant signals on the vertical and radial components, respectively. We compute

synthetic Green's functions for the vertical and the radial components by using wavenumber integration method (Herrmann 2013). The source is a vertical force. The source and receiver are 1 m below the seafloor at 71 m depth and the distance between them is 10 km.

Figs 4(a) and (b) show the phase and group velocities for the inverted Valhall model. The magenta line (Fig. 4a) indicates the lowest S-wave velocity at Valhall below seafloor (380 m s^{-1}, Fig. 3d). Following Biot (1952), Scholte wave phase velocity is lower than the lowest velocity, that is 380 m s^{-1}. Therefore, the fundamental mode is a Scholte wave for periods below 0.9 s, and it is a Rayleigh wave for period above 0.9 s. Supporting Information Fig. S2 shows the corresponding vertical and radial eigenfunctions. At short periods (e.g. 0.4 and 0.8 s), the eigenfunction amplitude is maximum at 70 m, that is at the ocean–sediment boundary, and decreases exponentially on both sides of the interface as expected for Scholte waves. At longer periods (1.2 and 1.6 s), eigenfunction amplitude is no more concentrated at the interface, but it is large from the surface down to a given depth that increases with increasing period. Higher modes ($n = 1$–8 in Fig. 4a) are all Rayleigh waves as the velocities of higher modes are higher than the lowest velocity.

Fig. 4 shows that there are up to nine modes that contribute in the period range of interest. Synthetic seismograms are plotted in Figs 4(c) and (e) for the vertical and radial components, respectively. All seismograms are filtered between 0.3 and 1.75 Hz. For both the vertical and radial components, the second to eight higher mode amplitudes are negligible.

On the vertical component, the fundamental mode is stronger than all other modes (Fig. 4d). In the frequency range 0.3 to 1.75), the first higher mode has signal of one order smaller magnitude than the fundamental mode. On the radial component, (Fig. 4e), the first overtone signal is four times larger than the fundamental mode signal. It is consistent with what we observed from the real data set for the vertical and radial components.

For comparison, we also compute velocities and synthetic seismograms for a model without the sediment layer, see Appendix A, Fig. A1). We observe that the fundamental mode signal is stronger than all other modes in the spectrum for the vertical as well as for the radial components.

Therefore, based on these observations, we can confidently suggest that few hundred metres of low velocity sediments below the 70 m water layer play an important role for the different amplitude of the fundamental mode with respect to the first overtone on vertical and radial components at Valhall. It is consistent with results on land from Savage *et al.* (2013), who observed stronger first-higher mode on radial component in the case of 1.5 km thick sedimentary layer.

5 AMBIENT NOISE SURFACE WAVE TOMOGRAPHY OF THE FUNDAMENTAL MODE AND FIRST OVERTONE

Using data and modelling, we have shown that the first overtone signal on RR component is stronger than the fundamental mode in the presence of a water layer with a sedimentary layer underneath it. In that case, it is possible to investigate the shallow structure deeper than if only the fundamental mode can be measured. We use F–K filtering to extract the first overtone from the RR component CCs. We apply an Eikonal tomography (Lin *et al.* 2009) to compute phase velocity maps at different periods (see Appendix B, Fig. B1). We extract the local dispersion curves from the 2-D phase velocity

maps computed at different periods for the fundamental mode and first overtone and invert them jointly by using the method described in Section 3. At every location, 25 000 models are tested for local dispersion curves. Fig. 5 shows the velocity–depth slices at different depths (at 120, 600 and 900 m) when using only the fundamental mode (Figs 5a, b and c, respectively) and using the fundamental mode along with the first overtone (Figs 5d, e and f, respectively). The paleochannels are visible at 120 m depth [indicated with the dotted lines and rectangle in Figs 5(a), (d), already obtained in FWI results of active source seismic data (Sirgue *et al.* 2010a)]. A low velocity anomaly starts at the depth of 600 m and becomes strong at 900 m depth (indicated with the ellipses in Figs 5e and f) in the middle of the map, which could be related to the gas cloud observed in the P-wave velocity depth-slice at 1050 m below the sea level obtained from FWI (Sirgue *et al.* 2009, 2010a). In principle, S-wave velocity should not represent any anomaly related to gas (Minshull *et al.* 1994). But for the isotropic inversion in S-wave velocity model, we get low velocity anomaly that could be related to gas. The anisotropic phase velocity is not only sensitive to V_{SV} but also to V_{PH} and V_{PV} (Montagner & Nataf 1986). Hence, it might be possible that the anomaly we observe in S-wave could be due to the decrease in P-wave velocity, which has been mapped in the V_{SV} inversion result. One can observe that this low velocity anomaly is enhanced after using the first overtone data in the inversion, which confirms the importance of using first overtone to improve the depth resolution.

6 DISCUSSION AND CONCLUSIONS

We have used just 6.5 hr of continuous recording of noise data from the Valhall LoFS network. We computed fundamental mode and first overtone average dispersion curves from the virtual gather of vertical and radial components, respectively.

These dispersion curves are inverted using a NA to get the average Valhall S-wave velocity structure down to ∼1 km. We showed that the inversion of the fundamental mode alone enables to retrieve the structure down to 700 m while adding the first overtone in the period range of interest enables to retrieve the structure down to ∼1 km. We computed eigenfunctions using the 1-D velocity model of Valhall (see Supporting Information Fig. S2). They confirm that the first overtone has sensitivity from the surface down to about 1 km. For this 1-D model, we also computed ZH-ratio, which shows that the particle motion is prograde at Valhall (Supporting Information Fig. S3).

Using synthetic seismograms in the period range 0.55 to 1.75 s, we demonstrated that the strongest signal is the fundamental mode on the vertical component and the first overtone on the radial component only in the presence of water and sediment layers. Without the sediment layer, the fundamental mode is the dominant signal on both vertical and radial component. It has strong implications in terms of seismic hazard assessment (in general, not only at Valhall).

The first overtone signal is retrieved from the radial component by F–K filtering and used to get the phase velocity distribution at different periods. The 2-D phase velocity maps are used to obtain the local dispersion curves at every grid points. The local dispersion curves are jointly inverted to obtain 3-D isotropic S-wave velocity structure down to ∼1 km after combining all 1-D vertical profiles. We observe geological structure like paleochannels, seafloor subsidence signature and a low velocity anomaly that is associated with the gas cloud present in the overburden of Valhall reservoir. The
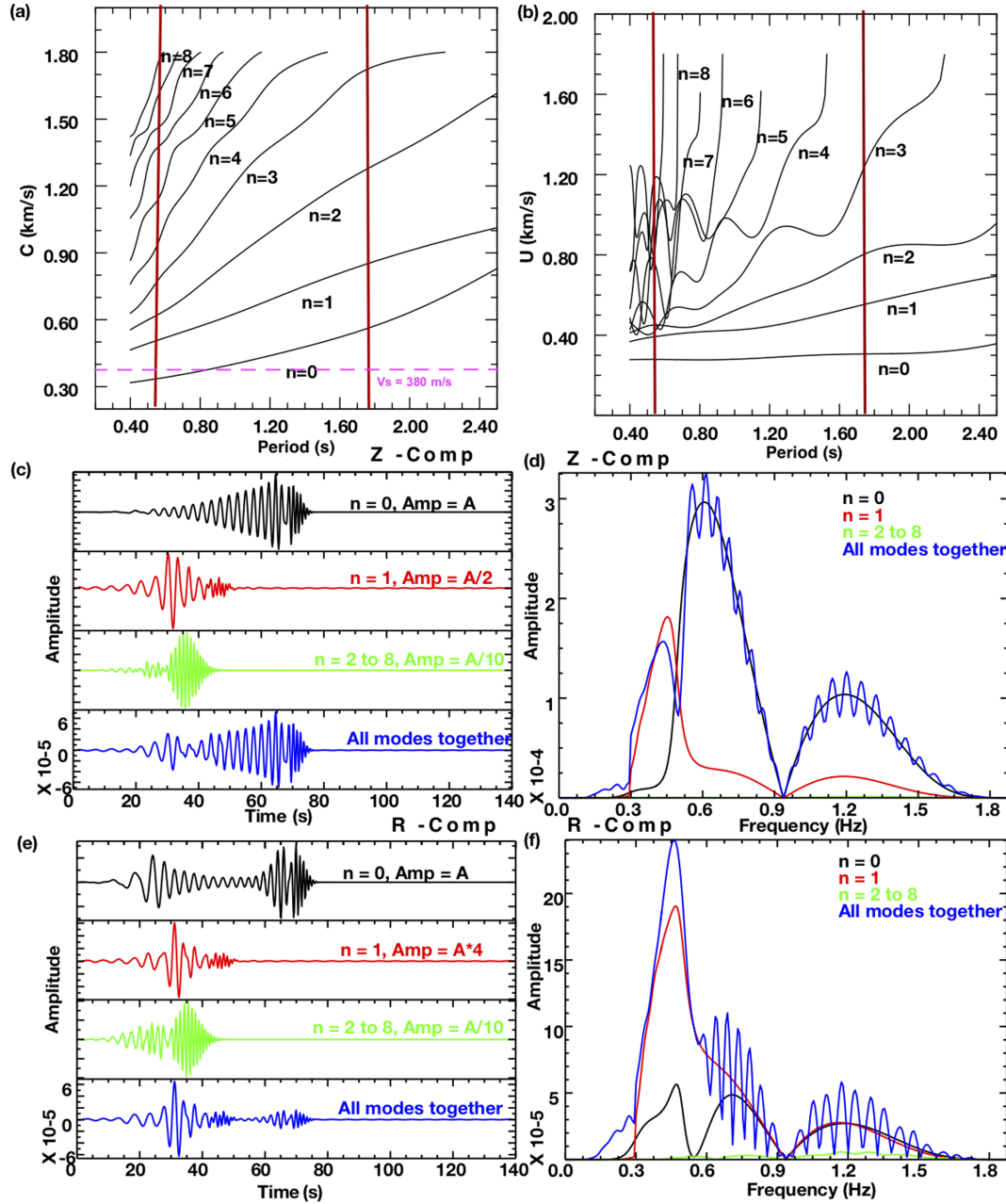
Figure 4. Phase (a) and group (b) velocities of the modes as a function of period computed for Valhall model. Red lines indicate the period range of interest between 0.55 and 1.75 s and magenta line indicates the lowest *S*-wave velocity below ocean in Valhall (Fig. 3d). Modes *n* = 0 to 8 have contribution for the synthetic seismograms in the period range of interest. Vertical (c) and radial (e) synthetic seismograms of the fundamental mode (black), first overtone (red), second to eight higher modes (green), and all modes together (blue). (d) and (f) are the corresponding spectra.

use of the first overtone strongly enhances the low velocity anomaly related to the gas cloud between 700 and 1000 m.

REFERENCES

Barkved, O., 2012. *Seismic Monitoring for Reservoir Delivery: From a Practitioner's Point of View,* EAGE.

Bensen, G.D., Ritzwoller, M.H. & Shapiro, N.M., 2008. Broadband ambient noise surface wave tomography across the United States, *J. geophys. Res.,* **113**(B5), doi:10.1029/2007JB005248.

Biot, M.A., 1952. The interaction of Rayleigh and Stoneley waves in the ocean bottom, *Bull. seism. Soc. Am.,* **42**(1), 81–93.
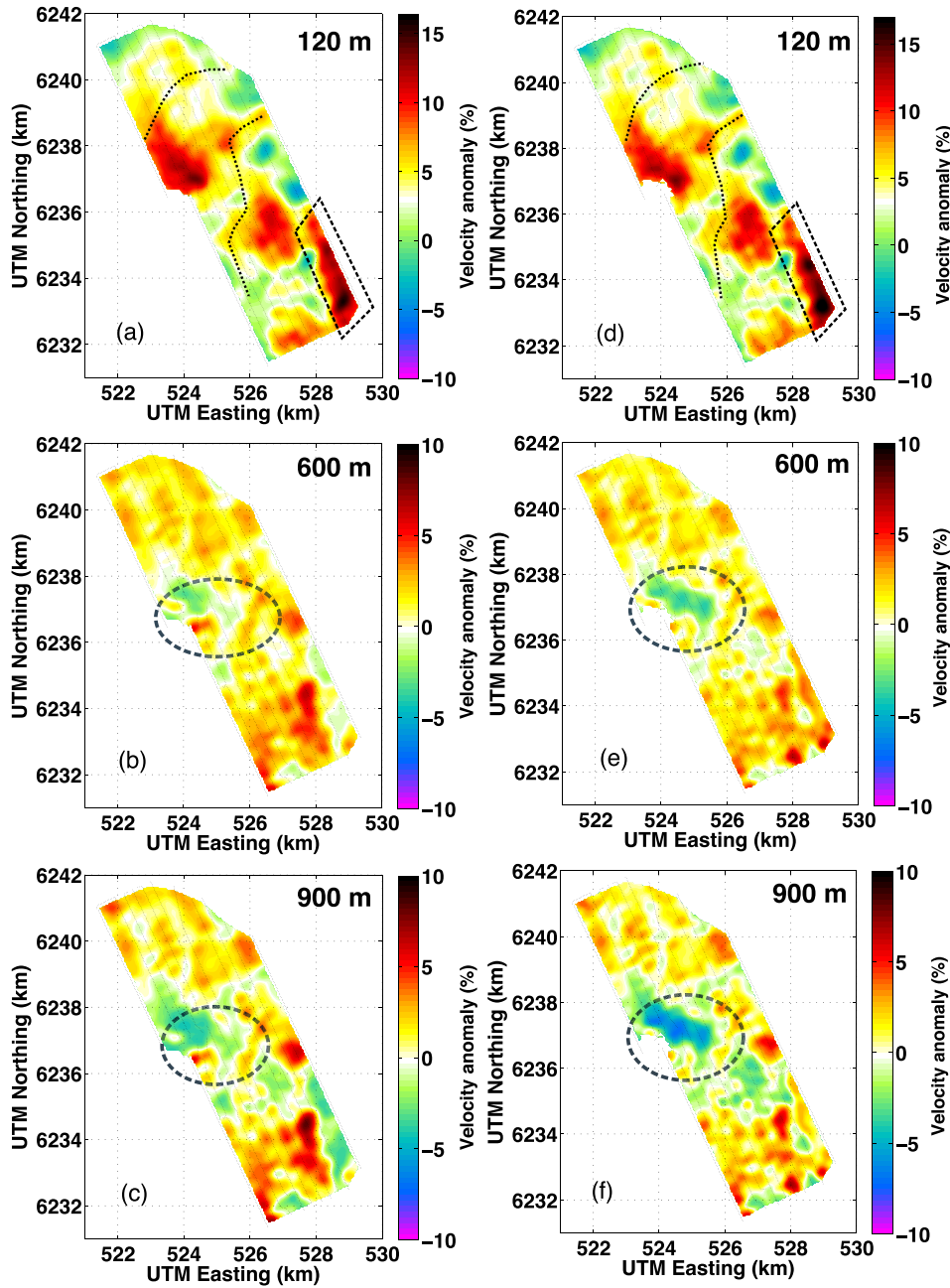
Figure 5. *S*-wave velocity anomaly depth slices at depth 120, 600 and 900 m. a–c: inversion of the fundamental mode only. d–f:, inversion of the fundamental mode and first overtone. The dashed lines and rectangle represent paleochannels (Sirgue *et al.* 2010). The low velocity anomaly at 900 m (dashed ellipse) is enhanced by joint inversion of first overtone and fundamental mode. This slow velocity anomaly is visible from 600 m depth down to 900 m depth.

Boaga, J., Cassiani, G., Strobbia, C.L. & Vignoli, G., 2013. Mode misidentification in Rayleigh waves: Ellipticity as a cause and a cure, *Geophysics,* **78**(4), 1–12.

Brocher, T.M., 2005. Empirical relations between elastic wavespeeds and density in the Earth's crust, *Bull. seism. Soc. Am.,* **95**(6), 2081–1092.

Castagna, J.P., Batzle, M.L. & Eastwood, R.L., 1985. Relationships between compressional-wave in elastic silicate rocks and shear-wave velocities, *Geophysics,* **50**(4), 571–581.

de Ridder, S., 2011. Ambient seismic noise tomography at Valhall, in *SEG Expanded Abstract,* pp. 1597–1601.

de Ri dder S.A, .L. & Biondi, B.L. dder S.A, 2013. Daily reservoir-scale subsurface monitoring using ambient seismic noise, *Geophys. Res. Lett.,* **40**(12), 2969–2974.

d e Ridder S., A.L., Biondi, B.L. & Clapp, R.G. e Ridder S., 2014. Time-lapse seismic noise correlation tomography at Valhall, *Geophys. Res. Lett.,* **41**(17), 6116–6122.

de Ridder S.A.&, L. Ridder S.A., 2014. Passive seismic surface-wave interferometry for reservoir-scale imaging.

Draganov D., Wapenaar K., Mulder W., Singer J., Verdel A., 2007. Retrieval of reflections from seismic background-noise measurements, *Geophys. Res. Lett.,* **34**, L04305., doi:10.1029/2006GL028735.

Draganov, D., Campman, X., Thorbecke, J., Verdel, A. & Wapenaar, K., 2013. Seismic exploration-scale velocities and structure from ambient seismic noise (>1 hz), *J. geophys. Res.,* **118,** 4345–4360.

Ekström, G., Abers, G. & Webb, S., 2009. Determination of surface-wave

phase velocities across USArray from noise and Aki's spectral formulation, *Geophys. Res. Lett.,* **36**(18), doi:10.1029/2009GL039131.

Gabriels, P., Snieder, R. & Nolet, G., 1987. In Situ Measurements of Shear-Wave Velocity in Sediments with Higher-Mode Rayleigh waves, *Geophys. Prospect.,* **35**, 187–196.

Gouédard, P. *et al.*, 2008. Cross-correlation of random fields: mathematical approach and applications, *Geophys. Prospect.,* **56**(3), 375–393.

Gualtieri, L., Stutzmann, E., Capdeville, Y., Farra, V., Mangeney, A. & Morelli, A., 2015. On the shaping factors of the secondary microseismic wave field, *J. geophys. Res.,* **120**(9), 6241–6262.

Haned, A., Stutzmann, E., Schimmel, M., Kiselev, S., Davaille, A. & Yelles-Chaouche, A., 2016. Glo bal tomography using seismic hum, *Geophys. J. Int.,* **204**(2), 1222–1236.

Harmon, N., Forsyth, D. & Webb, S., 2007. Using ambient seismic noise to determine short-period phase velocities and shallow shear velocities in young oceanic lithosphere, *Bull. seism. Soc. Am.,* **97**(6), 2009–2023.

Hasselman, D.P.H., 1963. Elastic energy at fracture and surface energy as design criteria for thermal shock. *J. Am. Ceram. Soc.,* **46**(11), 535–540.

Herrmann, R.B., 2013. Computer Programs in Seismology: An Evolving Tool for Instruction and Research, *Seismol. Res. Lett.,* **84**(6), 1081–1088.

Herrmann, R.B. & Ammon, C., 2004. Surface waves, receiver functions and crustal structure, in *Computer Programs in Seismology,* pp. 133, 135.

Kimman, W.P. & Trampert, J., 2010. Approximations in seismic interferometry and their effects on surface waves, *Geophys. J. Int.,* **182**(1), 461–476.

Lin, F., Ritzwoller, M. & Snieder, R., 2009. Eikonal tomography: surface wave tomography by phase front tracking across a regional broad-band seismic array, *Geophys. J. Int.,* **177**(3), 1091–1110.

Longuet-Higgins, M., 1950. A theory of the origin of microseisms, *Phil. Trans. R. Soc. A,* **243**(857), 1–35.

Minshull, T.A., Singh, S.C. & Westbrook, G.K., 1994. Seismic velocity structure at a gas hydrate reflector, offshore western Colombia, from full waveform inversion, *J. geophys. Res.,* **99**(B3), 4715–4734.

Montagner, J. & Nataf, H., 1986. A simple method for inverting the azimuthal anisotropy of surface waves, *J. geophys. Res.,* **91**(B1), 511–520.

Mordret, A., Shapiro, N.M., Singh, S., Roux, P., Montagner, J.P. & Barkved, O., 2013a. Azimuthal anisotropy at Valhall: The Helmholtz equation approach, *Geophys. Res. Lett.,* **40**(11), 2636–2641.

Mordret, A., Shapiro, N.M., Singh, S., Roux, P. & Barkved, O., 2013b. Helmholtz tomography of ambient noise surface wave data to estimate Scholte wave phase velocity at Valhall Life of the Field, *Geophysics,* **78**(2), WA99–WA109.

Mordret, A., Landés, M., Shapiro, N.M., Singh, S.C., Roux, P. & Barkved, O.I., 2013c. Near-surface study at the valhall oil field from ambient noise surface wave tomography, *Geophys. J. Int.,* **193**(3), 1627–1643.

Mordret, A., Landès, M., Shapiro, N.M., Singh, S. & Roux, P., 2014a. Ambient noise Surface wave tomography to determine the shallow shear velocity structure at Valhall: depth inversion with a Neighbourhood Algorithm, *Geophys. J. Int.,* **198**(3), 1514–1525.

Mordret, A., Shapiro, N.M. & Singh, S., 2014b. Seismic noise-based time-lapse monitoring of the overburden Valhall, *Geophys. Res. Lett.,* **41**(4), 4945–4952.

Moschetti, M.P., Ritzwoller, M.H. & Shapiro, N.M., 2007. Surface wave tomography of the western United States from ambient seismic noise: Rayleigh wave group velocity maps, *Geochem. Geophys. Geosyst.,* **8**(8), 1–10.

Munns, J.W., 1985. The Valhall Field: a geological overview, *Mar. Pet. Geol.,* **2**(1), 23–43.

Nishida, K., Kawakatsu, H. & Obara, K., 2008. Three-dimensional crustal S wave velocity structure in Japan using microseismic data recorded by Hi-net tiltmeters, *J. geophys. Res.,* **113**(10), doi: 10.1029/2007JB005395.

Nishida, K., Montagner, J.-P. & Kawakatsu, H., 2009. Global surface wave tomography using seismic hum, *Science,* **326**(5949), 112–112.

Priestley, K., Orcutt, J.A. & Brune, J.N., 1980. Higher-mode surface waves and structure of the Great Basin of Nevada and western Utah, *J. geophys. Res.,* **85**(B12), 7166–7174.

Rivet, D., Campillo, M., Sanchez-Sesma, F., Shapiro, N.M. & Singh, S.K., 2015. Identification of surface wave higher modes using a methodology based on seismic noise and coda waves, *Geophys. J. Int.,* **203**(2), 856–868.

Roux, P. & Sabra, K., 2005. Ambient noise cross correlation in free space: Theoretical approach, *J. acoust. Soc. Am.,* **117**(1), 79–84.

Roux, P., Kuperman, W. & Group, N., 2004. Extracting coherent wave fronts from acoustic ambient noise in the ocean, *J. acoust. Soc. Am.,* **116**(4), 1995–2003.

Sambridge, M., 1999. Geophysical inversion with a neighborhood algorithm - II. Appraising the whole, *Geophys. J. Int.,* **138**(3), 727–746.

Savage, M., Lin, F.-C. & Townend, J., 2013. Ambient noise cross-correlation observations of fundamental and higher-mode Rayleigh wave propagation governed by basement resonance, *Geophys. Res. Lett.,* **40**(14), 3556–3561.

Scholte, J.G., 1946. The Range of Existence of Rayleigh.

Scholte, G., 1947. The Range of Existence of Rayleigh and Stoneley Waves, *Geophys. Suppl. Mon. Not. R. Astron. Soc.,* **5**(5), 120–126.

Scholte, J.G.J., 1958. *Rayleigh Waves in Isotropic and Anisotropic Elastic Media*, Vol. 72, pp. 9–43, Mededelingen en verhandelingen, KNMI, Staatsdr.- en Uitgeverijledrijf.

Shapiro, N.M. & Campillo, M., 2004. Emergence of broadband Rayleigh waves from correlations of the ambient seismic noise, *Geophys. Res. Lett.,* **31**(7), doi:10.1029/2004GL019491.

Shapiro, N.M., Campillo, M., Stehly, L. & Ritzwoller, M.H., 2005. Highresolution surface-wave tomography from ambient seismic noise, *Science,* **307**(5715), 1615–1618.

Sirgue, L., Bakverd, O.I., Van Gestel, J.P., Askim, O.J. & Kommendal, J.H., 2009. 3D Waveform Inversion on Valhall Wide-azimuth OBC, in *71st EAGE Conf.,* Amsterdam, The Netherlands, 8–11 June, (June 2009), U038.

Sirgue, L., Barkved, O.I., Dellinger, J., Etgen, J., Albertin, U. & Kommedal, J.H., 2010a. Full waveform inversion: The next leap forward in imaging at Valhall, *First Break,* **28**(4), 65–70.

Sirgue, T., Barkved, O., Dellinger, J., Etgen, J. & Albertin, U., 2010b. Thematic set: Full waveform inversion: The next leap forward in imaging at Valhall, *First Break,* **28**(4), 65–70.

Snieder, R., 2004. Extracting the Green's function from the correlation of coda waves: a derivation based on stationary stage, *Phys. Rev. E,* **69**(4), 046610, doi:10.1103/PhysRevE.69.046610.

Snieder, R., 2006. The theory of coda wave interferometry, *Pure appl. Geophys.,* **163**(2–3), 455–473.

Socco, L.V. & Strobbia, C., 2004. Surface-wave method for near-surface characterization: a tutorial, *Near Surf. Geophys.,* **2**(4), 165–185.

Tanimoto, T. & Rivera, L., 2005. Prograde Rayleigh wave particle motion. *Geophys. J. Int.,* **162**(2), 399–405.

Tomar, G., Shapiro, N.M., Singh, S., Montagner, J. & Mordret, A., 2015a. Radial anisotropy in Valhall from ambient noise surface wave tomography of Scholte and Love wave, *SEG Tech. Progr. Expand. Abstr.,* **34**, 2342–2347.

Tomar, G., Shapiro, N.M., Mordret, A., Singh, S. & Montagner, J., 2015b. Noise based seismic tomography at Valhall oil filed using Scholte and Love waves, in 77th *EAGE Conference and Exhibition Madris,* Extended abstract, WS_{11}-Bo_1.

Tomar, G., Mordret, A., Shapiro, N.M., Singh, S. & Montagner, J., 2016. Radial anisotropy in Valhall: ambient noise based study of Scholte and Love wave, *Geophys. J. Int.,* **208**(3), 1524–1539.

Viens, L., Koketsu, K., Miyake, H., Sakai, S. & Nakagawa, S., 2016. Basin-scale Green's functions from the ambient seismic field recorded by MeSO-net stations, *J. geophys. Res.,* **121**(4), 2507–2520.

Wapenaar, K., 2004. Retrieving the elastodynamic Green's function of an arbitrary inhomogeneous medium by cross correlation, *Phys. Rev. Lett.,* **93**(25).

Wapenaar, K. & Fokkema, J., 2006. Green's function representations for seismic interferometry, *Geophysics,* **71**(4), SI33–SI46.

Wathelet, M., Jongmans, D. & Ohrnberger, M., 2004. Surface wave inversion using a direct search algorithm and its application to ambient vibration measurements, *Near surface geophysics,* **2**(4), 211–221.

Weaver, R. & Lobkis, O., 2001a. On the emergence of the Green's function in the correlations of a diffuse field, *J. acoust. Soc. Am.,* **110**(6), 3011–3017.

Weaver, R. & Lobkis, O., 2001b. Ultrasonics without a source: thermal

fluctuation correlations at MHz frequencies, *Phys. Rev. Lett.,* **87**(3), 134–301.

Wessel, P. & Bercovici, D., 1998. Interpolation with splines in tension: a Grees's function approach, *Math. Geol.,* **30**(1), 77–93.

Yang, Y., Ritzwoller, M.H., Levshin, A.L. & Shapiro, N.M., 2007. Ambient noise Rayleigh wave tomography across Europe, *Geophys. J. Int.,* **168**(1), 259–274.

SUPPORTING INFORMATION

Supplementary data are available at *GJI* online.

Figure S1. Virtual gather (a) and its F–K spectrum (b) of HH component. All correlations computed for HH component are stacked and averaged in 10 m interstation distance bins. Blue and magenta colours are the fundamental mode and the first overtone dispersion curves, respectively, that were picked from the F–K spectrum of ZZ and RR component virtual gathers, respectively (see Fig. 2).

Figure S2. Vertical and radial eigenfunctions are computed for the fundamental mode at periods 0.4 s (a, e), 0.8 s (b, f) 1.2 s (c, g) and 1.6 s (d, h) respectively, and for first overtone at periods 0.4 s (i, m), at 0.8 s (j, n) 1.2 s (k, o) and 1.5 s (l, p), respectively. The black horizontal line indicates the interface (water–sediment interface). Vertical and horizontal ZH-ratio is computed at the interface ($\sim$70 m).

Figure S3. ZH-ratio is computed from eigenfunctions obtained at different periods (Fig. S2). Particles have prograde motion for period range 0.3–1.6 s.

Please note: Oxford University Press is not responsible for the content or functionality of any supporting materials supplied by the authors. Any queries (other than missing material) should be directed to the corresponding author for the paper.

APPENDIX A: SYNTHETIC SEISMOGRAMS IN A MODEL WITHOUT SEDIMENT LAYER

We remove the sediment layer from the Valhall model and compute a synthetic seismogram at 10 km distance between source and receiver. The source and the receiver are located 1 m below the surface. For this model, Figs A1 (a) and (b) show phase and group velocities for the first eight modes in the period range of interest, between 0.55 and 1.75 s. Figs A1 (c) and (e) show the synthetic seismograms of the eight modes for the vertical and radial component, respectively. Corresponding spectra are plotted in Figs A1 (d) and (f).

Figs A1 (c) and (d) show that, on the vertical component, the fundamental mode signal is stronger than all other modes and that the second to eight modes have amplitude close to zero. Figs A1 (e) and (f) show that, on the radial component, the dominant signal is also the fundamental mode. This is the classical amplitude ratio of modes on vertical and radial components. In the case of Vahlall, the sediment layers play an important role for shaping the seismic wavefield. Interference of waves propagating in these layers modify the mode relative amplitude and we observe that amplitude of the first overtone becomes larger than that of the fundamental mode on the radial component (Fig. 4).

APPENDIX B: TOMOGRAPHY OF THE FUNDAMENTAL MODE AND FIRST OVERTONE SCHOLTE/RAYLEIGH WAVES

CCs between all the possible pair of sensors of ZZ component are used to compute the fundamental mode phase velocity. Eikonal tomography is used to construct 2-D phase velocity maps at different periods. We use the method discussed in Mordret *et al.* (2013b) and Tomar *et al.* (2016): first, the frequency-dependent phase travel times are measured for each interstation noise CC and interpolated on to a regular grid of 50 × 50 m across the whole Valhall array, using spline in-tension interpolation (Wessel & Bercovici 1998). The in-tension coefficient takes care of smoothness of the interpolated surface between the data points. Second, we compute the phase-slowness maps for all 2320 receivers by taking the gradient of interpolated phase travel time in this period range. Third, the 2-D slowness maps are constructed by averaging all 2320 maps and their uncertainties are estimated by taking their standard deviation. Finally, we invert the slowness map to get a 2-D phase velocity distribution for the whole Valhall array at each period.

Figs B1(a) and (b) show the phase velocity maps at two different periods (0.7 and 1.4 s, respectively). We see high velocity anomaly indicated with the dotted curve that corresponds to the shallow paleochannels as interpreted by BP author (see, Sirgue *et al.* 2010a). In the Southeast part of the area, a big paleochannel is clearly visible. Similar results were obtained by Mordret *et al.* (2013b), de Ridder *et al.* (2014) and Tomar *et al.* (2016).

To extract the first overtone of Rayleigh waves, we use RR component CCs and apply F–K filter to distinguish it from fundamental mode. These filtered waveforms are used to construct 2-D phase-velocity maps using the Eikonal tomography using the method is described above. The first overtone velocity is higher than fundamental mode. Figs B1(c), (d) show, the 2-D phase-velocity maps at two different periods (1.2 and 1.4 s, respectively).

In the middle of the first overtone phase-velocity maps (Figs B1c and d), we can see a low velocity anomaly (indicated with the black ellipses,). This velocity anomaly may correspond to deeper structure than what is observed on the fundamental mode phase velocity maps. The phase-velocity maps of first overtone are constructed from 1 to 1.5 s at an interval of 0.1 s and jointly inverted with the fundamental mode phase velocity maps for obtaining the 3-D velocity variation (Fig. 5).
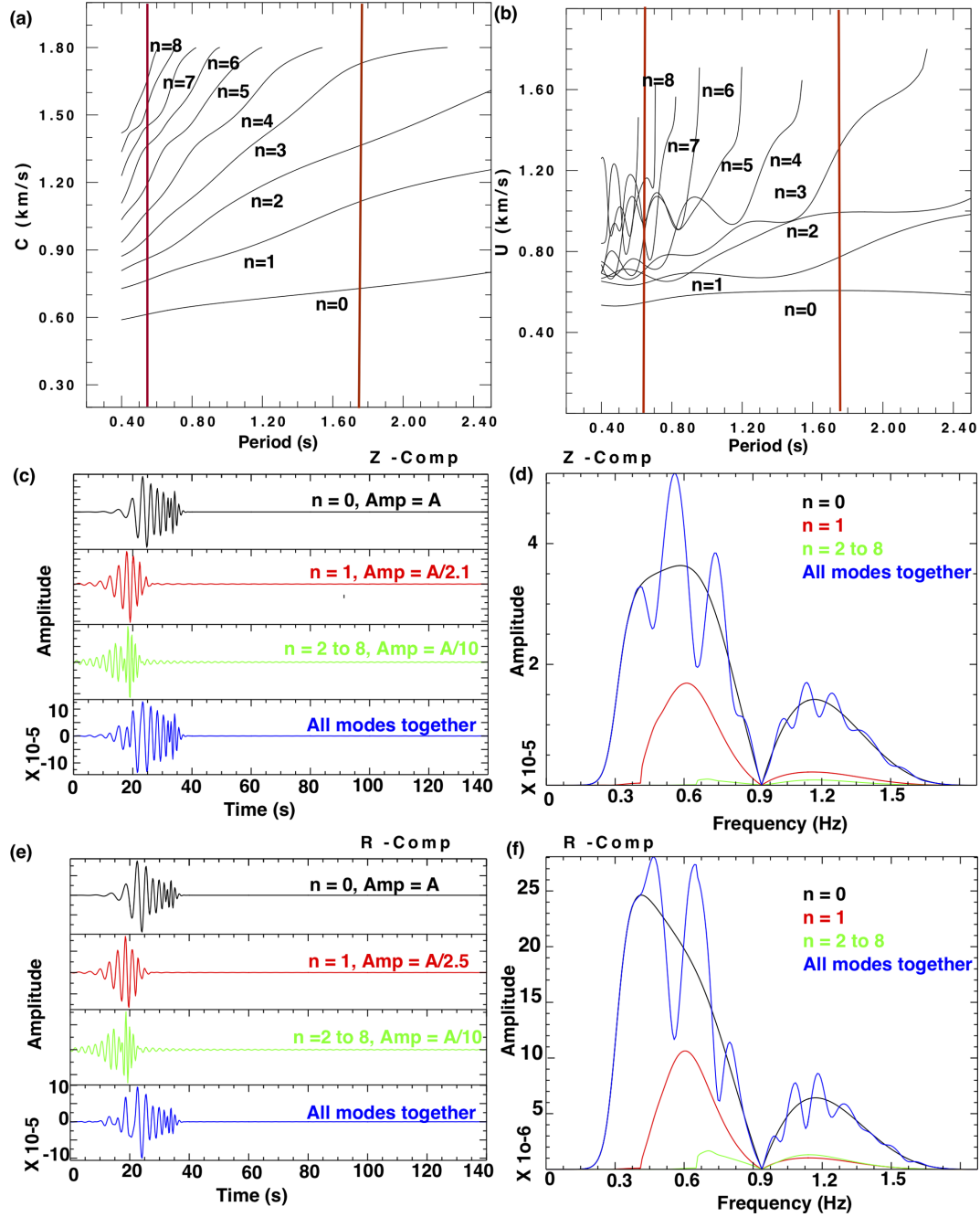
Figure A1. Phase (a) and group (b) velocities of the modes as a function of period computed for Valhall model without sedimentary layer. Red lines indicate the period range of interest between 0.55 and 1.75 s. Modes $n = 0$ to 8 have contribution for the synthetic seismograms in the period range of interest. Vertical (c) and radial (e) synthetic seismograms of the fundamental mode (black), first overtone (red), second to eight higher modes (green), and all modes together (blue). (d) and (f) are the corresponding spectra.
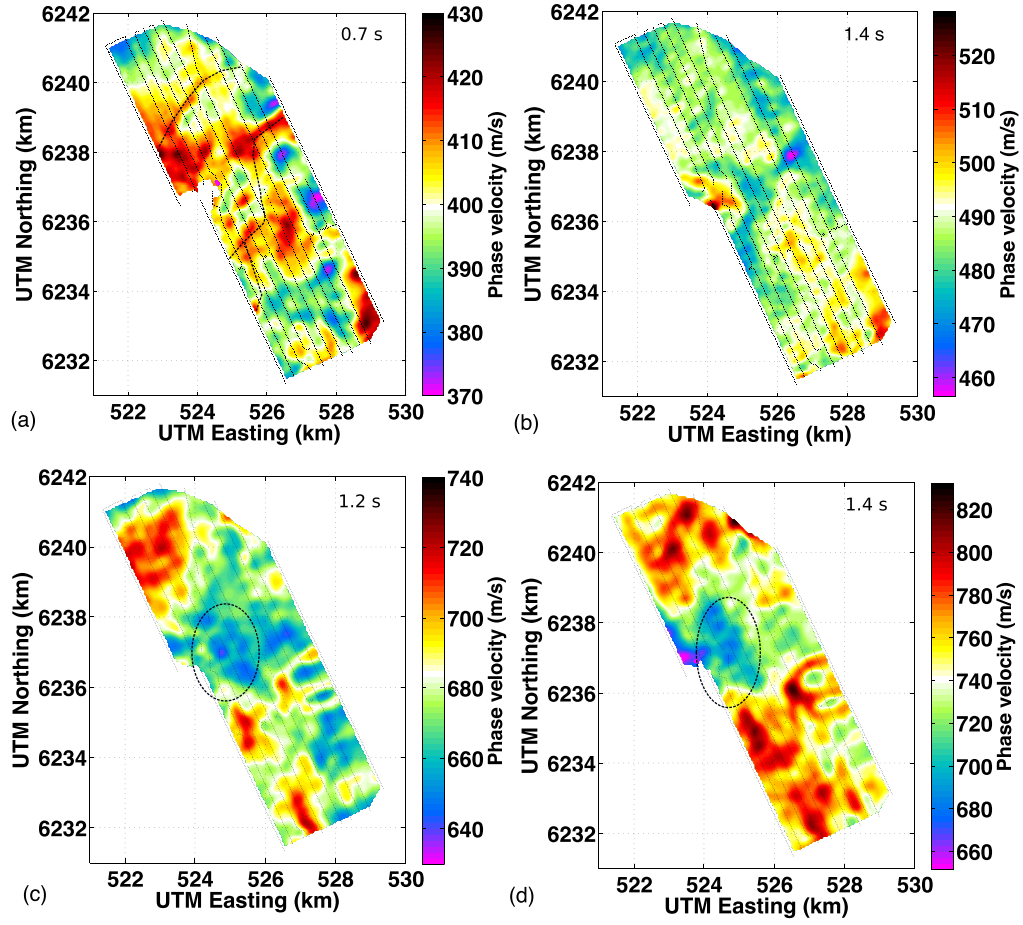
Figure B1. Phase-velocity maps of fundamental mode at periods of 0.7 s (a) and at 1.4 s (b). The dotted lines indicate the paleochannels in shallow part of Valhall overburden. Phase-velocity maps of first overtone at periods of 1.2 s (c) and at 1.4 s (d). The dotted ellipses indicate the low velocity anomaly in Valhall overburden.

Key words

Authors are requested to choose key words from the list below to describe their work. The key words will be printed underneath the summary and are useful for readers and researchers. Key words should be separated by a semi-colon and listed in the order that they appear in this list. An article should contain no more than six key words.

COMPOSITION and PHYSICAL PROPERTIES
Composition and structure of the continental crust
Composition and structure of the core
Composition and structure of the mantle
Composition and structure of the oceanic crust
Composition of the planets
Creep and deformation
Defects
Elasticity and anelasticity
Electrical properties
Equations of state
Fault zone rheology
Fracture and flow
Friction
High-pressure behaviour
Magnetic properties
Microstructure
Permeability and porosity
Phase transitions
Plasticity, diffusion, and creep

GENERAL SUBJECTS
Core
Gas and hydrate systems
Geomechanics
Geomorphology
Glaciology
Heat flow
Hydrogeophysics
Hydrology
Hydrothermal systems
Instrumental noise
Ionosphere/atmosphere interactions
Ionosphere/magnetosphere interactions
Mantle processes
Ocean drilling
Structure of the Earth
Thermochronology
Tsunamis
Ultra-high pressure metamorphism
Ultra-high temperature metamorphism

GEODESY and GRAVITY
Acoustic-gravity waves
Earth rotation variations
Geodetic instrumentation
Geopotential theory
Global change from geodesy
Gravity anomalies and Earth structure
Loading of the Earth
Lunar and planetary geodesy and gravity
Plate motions
Radar interferometry
Reference systems
Satellite geodesy
Satellite gravity
Sea level change
Seismic cycle

Space geodetic surveys
Tides and planetary waves
Time variable gravity
Transient deformation

GEOGRAPHIC LOCATION
Africa
Antarctica
Arctic region
Asia
Atlantic Ocean
Australia
Europe
Indian Ocean
Japan
New Zealand
North America
Pacific Ocean
South America

GEOMAGNETISM and ELECTROMAGNETISM
Archaeomagnetism
Biogenic magnetic minerals
Controlled source electromagnetics (CSEM)
Dynamo: theories and simulations
Electrical anisotropy
Electrical resistivity tomography (ERT)
Electromagnetic theory
Environmental magnetism
Geomagnetic excursions
Geomagnetic induction
Ground penetrating radar
Magnetic anomalies: modelling and
    interpretation
Magnetic fabrics and anisotropy
Magnetic field variations through time
Magnetic mineralogy and petrology
Magnetostratigraphy
Magnetotellurics
Marine electromagnetics
Marine magnetics and palaeomagnetics
Non-linear electromagnetics
Palaeointensity
Palaeomagnetic secular variation
Palaeomagnetism
Rapid time variations
Remagnetization
Reversals: process, time scale,
    magnetostratigraphy
Rock and mineral magnetism
Satellite magnetics

GEOPHYSICAL METHODS
Downhole methods
Fourier analysis
Fractals and multifractals
Image processing
Instability analysis

Interferometry
Inverse theory
Joint inversion
Neural networks, fuzzy logic
Non-linear differential equations
Numerical approximations and analysis
Numerical modelling
Numerical solutions
Persistence, memory, correlations, clustering
Probabilistic forecasting
Probability distributions
Self-organization
Spatial analysis
Statistical methods
Thermobarometry
Time-series analysis
Tomography
Waveform inversion
Wavelet transform

PLANETS
Planetary interiors
Planetary volcanism

SEISMOLOGY
Acoustic properties
Body waves
Coda waves
Computational seismology
Controlled source seismology
Crustal imaging
Earthquake dynamics
Earthquake early warning
Earthquake ground motions
Earthquake hazards
Earthquake interaction, forecasting,
    and prediction
Earthquake monitoring and test-ban
    treaty verification
Earthquake source observations
Guided waves
Induced seismicity
Interface waves
Palaeoseismology
Rheology and friction of fault zones
Rotational seismology
Seismic anisotropy
Seismic attenuation
Seismic instruments
Seismic interferometry
Seismicity and tectonics
Seismic noise
Seismic tomography
Site effects
Statistical seismology
Surface waves and free oscillations
Theoretical seismology
Tsunami warning

Volcano seismology
Wave propagation
Wave scattering and diffraction

TECTONOPHYSICS
Backarc basin processes
Continental margins: convergent
Continental margins: divergent
Continental margins: transform
Continental neotectonics
Continental tectonics: compressional
Continental tectonics: extensional
Continental tectonics: strike-slip and transform
Cratons
Crustal structure
Diapirism
Dynamics: convection currents, and mantle
    plumes
Dynamics: gravity and tectonics
Dynamics: seismotectonics
Dynamics and mechanics of faulting
Dynamics of lithosphere and mantle
Folds and folding
Fractures, faults, and high strain
    deformation zones
Heat generation and transport
Hotspots

Impact phenomena
Intra-plate processes
Kinematics of crustal and mantle deformation
Large igneous provinces
Lithospheric flexure
Mechanics, theory, and modelling
Microstructures
Mid-ocean ridge processes
Neotectonics
Obduction tectonics
Oceanic hotspots and intraplate volcanism
Oceanic plateaus and microcontinents
Oceanic transform and fracture zone processes
Paleoseismology
Planetary tectonics
Rheology: crust and lithosphere
Rheology: mantle
Rheology and friction of fault zones
Sedimentary basin processes
Subduction zone processes
Submarine landslides
Submarine tectonics and volcanism
Tectonics and climatic interactions
Tectonics and landscape evolution
Transform faults
Volcanic arc processes

VOLCANOLOGY
Atmospheric effects (volcano)
Calderas
Effusive volcanism
Eruption mechanisms and flow emplacement
Experimental volcanism
Explosive volcanism
Lava rheology and morphology
Magma chamber processes
Magma genesis and partial melting
Magma migration and fragmentation
Mud volcanism
Physics and chemistry of magma bodies
Physics of magma and magma bodies
Planetary volcanism
Pluton emplacement
Remote sensing of volcanoes
Subaqueous volcanism
Tephrochronology
Volcanic gases
Volcanic hazards and risks
Volcaniclastic deposits
Volcano/climate interactions
Volcano monitoring
Volcano seismology